Plasma Physics and Controlled Fusion

PAPER • OPEN ACCESS

Doppler coherence imaging of divertor and SOL flows in ASDEX upgrade and Wendelstein 7-X

To cite this article: D Gradic *et al* 2018 *Plasma Phys. Control. Fusion* **60** 084007

View the article online for updates and enhancements.

Related content

- Review Article
M Hirsch, J Baldzuhn, C Beidler et al.
- EMC3-EIRENE modelling of edge plasma and impurity emissions compared with the liquid lithium limiter experiment on EAST
T. Xie, S.Y. Dai, G.Z. Zuo et al.
- Three-dimensional simulations of edge impurity flow obtained by the vacuum ultraviolet emission diagnostics in the Large Helical Device with EMC3-EIRENE
S.Y. Dai, T. Oishi, G. Kawamura et al.

IOP ebooks™

Bringing you innovative digital publishing with leading voices to create your essential collection of books in STEM research.

Start exploring the collection - download the first chapter of every title for free.

This content was downloaded from IP address 192.107.175.1 on 15/03/2019 at 10:33

OPEN ACCESS
IOP Publishing
Plasma Physics and Controlled Fusion
Plasma Phys. Control. Fusion **60** (2018) 084007 (12pp)
https://doi.org/10.1088/1361-6587/aac4d2

Doppler coherence imaging of divertor and SOL flows in ASDEX upgrade and Wendelstein 7-X

D Gradic[1], O P Ford[1], A Burckhart[2], F Effenberg[3], H Frerichs[3], R König[1], T Lunt[2], V Perseo[1], R C Wolf[1], ASDEX Upgrade Team[2], Wendelstein 7-X Team[1] and Eurofusion MST1 team[2,4]

[1] Max-Planck-Institut für Plasmaphysik, D-17491 Greifswald, Germany
[2] Max-Planck-Institut für Plasmaphysik, D-85748 Garching, Germany
[3] Department of Engineering Physics, University of Wisconsin-Madison, WI 53706, United States of America

E-mail: dgradic@ipp.mpg.de

Received 1 January 2018, revised 18 April 2018
Accepted for publication 15 May 2018
Published 19 June 2018

Abstract

Measurement of ion dynamics is of great importance to the study of plasma exhaust and impurity particle flows in the scrape-off-layer (SOL) and divertor in magnetic confinement experiments. Doppler coherence imaging spectroscopy (CIS) is a passive optical diagnostic that produces 2D images of line-integrated ion flow velocity. Doppler CIS flow measurements of neutral deuterium and impurities were conducted for the first time in the divertor of the medium-sized tokamak experiment ASDEX Upgrade. A detailed sightline, emission and magnetic field analysis was undertaken to identify location and direction of flows. Under the assumption of toroidal axisymmetry, they revealed mainly parallel impurity flows in the proximity of the X-point and target plates on the order of 20 km s^{-1}. Two Doppler CIS systems are currently set up for the optimized stellarator Wendelstein 7-X (W7-X). The main task of this diagnostic will be the measurement of impurity ion flows in one of the island divertors of W7-X. EMC3-EIRENE simulations have been carried out to estimate the flow behaviour in the W7-X SOL.

Keywords: coherence imaging, divertor flows, ASDEX Upgrade

(Some figures may appear in colour only in the online journal)

1. Introduction

A Doppler coherence imaging spectroscopy (CIS) diagnostic was prepared and successfully implemented for impurity ion flow measurements in the divertor of the medium-sized tokamak ASDEX Upgrade (AUG). The CIS is a powerful tool in the study of (bulk) impurity and neutral transport in the SOL and divertor of high-temperature plasma experiments. It collects large quantities of flow data during a discharge with a single camera. Its velocity resolution can be adjusted to measure velocities of down to hundreds of meters per second [1]. The goal of the CIS in AUG as well as Wendelstein 7-X (W7-X) is to gain a fundamental understanding of the divertor and scrape-off-layer (SOL) impurity dynamics under diverse conditions, i.e. with various divertor regimes or magnetic configurations. This is particularly interesting for the magnetic island divertor in W7-X, for which many interesting predictions from the plasma edge code EMC3/EIRENE have been simulated and need to be experimentally investigated and confirmed. One such example is an impurity screening effect by the magnetic islands [2] that could reveal important aspects about the impurity transport from the SOL to the core. The question whether certain impurities travel away from or

[4] See author list in H. Meyer *et al* 2017 *Nucl. Fusion* **57** 102014.

Original content from this work may be used under the terms of the Creative Commons Attribution 3.0 licence. Any further distribution of this work must maintain attribution to the author(s) and the title of the work, journal citation and DOI.

 © 2018 IOP Publishing Ltd Printed in the UK

towards the divertor targets is an important one for both tokamaks and stellarator divertors; however, the application of the CIS in a high-temperature plasma experiment is challenging, since available calibration sources for prominent visible emission lines are scarce and not ideal.

High-quality, absolutely calibrated C III and He II flow measurements will be presented and rudimentarily interpreted in this work. The developed and applied CIS set-up for AUG serves as a guideline for a new Doppler CIS currently put together [3] in the optimized stellarator W7-X [4], and will be discussed while presenting the first Doppler CIS impurity flow measurements in AUG, which were obtained in a low-recycling divertor regime. Flow drive mechanisms of plasma and impurities in the SOL of tokamaks and stellarators are briefly described in section 2. In section 3, the general principle of the Doppler CIS is explained, followed by an overview of the AUG measurements and implications in section 4. An outlook on the expected flows in the W7-X SOL and divertor region is presented in section 5.

2. Impurity flow drive mechanisms in SOL and divertor plasmas

Preventing impurities from entering the confinement core is one of the crucial tasks of a divertor. In both tokamaks and stellarators, impurity transport in the SOL is based on the same fundamental mechanisms. For a collisional SOL and a sufficiently small impurity concentration, the impurity transport along the field lines is governed by a force balance ([5, 6], p.298):

$$\vec{F} = \frac{n_z Z^2}{m_i^{1/2} T_i^{3/2}} + \beta_i \frac{\mathrm{d}(k_B T_i)}{\mathrm{d}s} + m_z \frac{v_i - v_z}{\tau_s} + ZeE = 0. \tag{1}$$

The direction and magnitude of parallel impurity flows in the SOL and divertor depend on the balance between several counter-acting forces: an impurity pressure gradient (1st term), thermal ion temperature gradient (2nd), friction forces (3rd) and electric fields (4th). v_z is the impurity velocity, v_i the plasma ion velocity, τ_s the Spitzer stopping time (cf [6] and β_i a mass-dependent coefficient. The thermal temperature gradient force usually points upstream or away from the divertor target plates, whereas the friction with the main plasma flow is normally directed towards the divertor plates. Both forces are strongly dependent on the divertor parameters and the main plasma flow speed, v_i. For different divertor regimes, different impurity flow patterns might arise, e.g. for high collisionalities (e.g. high SOL upstream density, low temperatures), the friction force between the impurities and the background plasma flow becomes dominant, pushing the impurities towards the target plates. For large temperature gradients between the down and upstream SOL positions, the thermal gradient force, which points away from the (colder) target plates, increases. Due to the impurity source term, that pushes the impurities into regions of lower impurity density; no general statement can be made about the flow behavior of impurity species in e.g. different divertor regimes.

In a previous study [5], which investigated the differences between stellarator and tokamak divertor transport, it was shown that radial transport plays a more prominent role in the stellarator SOL. This is due to much larger connection lengths and counter-flowing transport channels, that are in close proximity to each other in an island topology with several X-points.

Significant perpendicular bulk impurity and plasma flow can be caused by classical drifts such as $\vec{E}_r \times \vec{B}$, $\vec{E}_\theta \times \vec{B}$ or $\vec{v}_{\mathrm{dia}} = -\vec{\nabla} p \times \vec{B}/(qnB^2)$ ('diamagnetic drift'). Electric fields in the SOL usually arise due to temperature gradients ([6], p.542). Poloidal $\vec{E}_r \times \vec{B}$-drifts can cause particle flow from the LFS to HFS [7], thereby contributing to higher densities in the HFS divertor in the case of low divertor densities [8]. Perpendicular impurity flows due to electric fields on the order of a few kV m^{-1} and diamagnetic drifts amount to flows up to a thousand meters per second, which is less than expected in the parallel direction.

The main plasma ion flow in the SOL is usually directed downstream towards the divertor target plates, which act like a particle sink for the plasma. It is primarily pressure-driven, arising due to poloidal transport asymmetries in the SOL according to [9, 10]. In tokamaks, poloidal pressure asymmetries occur due to the radial core transport distribution into the SOL. Usually, more particles are lost at the outer midplane because of bad curvature. Secondary (parallel) flows are generated by Pfirsch−Schlüter ion currents or the overall toroidal rotation of the core plasma [9]. It is therefore necessary to distinguish the main plasma ion flow from impurity particle flows, since they have different sources and are acted upon by different forces. If the friction force is not dominant, significant differences between the impurity and plasma flows may arise.

The general aim of the application of the Doppler CIS in AUG and W7-X is to investigate the impurity flow dynamics of diverse impurity species in varying plasma conditions, e.g. differing divertor regimes. This is still work in progress, and first results from AUG contain a limited set of data. For W7-X, Doppler CIS flow measurements are currently under way. A synthetic EMC3/EIRENE routine has been developed [11] to facilitate direct comparisons between the flow measurements and code predictions. First flow simulations of the routine for the Doppler CIS will be presented here as well.

3. Doppler coherence imaging spectroscopy

The Doppler coherence imaging diagnostic was proposed nearly three decades ago [12], and has subsequently undergone many alterations [13]. For AUG and the forthcoming W7-X Doppler CIS measurements, the spatial heterodyne technique is applied [14–16], where plasma images are recorded with a camera and modulated with a spatial periodic fringe signal. The fringes are produced by birefringent plates and encode spectral properties of the observed plasma

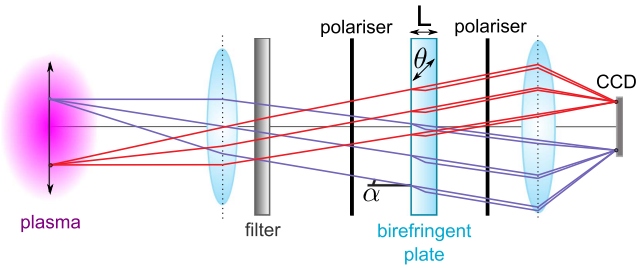

Figure 1. Schematic of the Doppler coherence imaging principle. α is the incidence angle of the light, θ the angle between the plate surface and the birefringent axis. In the set-up applied for AUG measurements; a birefringent α-BBO displacer plate ($\theta = 45°$) was used, sometimes in combination with a delay plate ($\theta = 0°$), not illustrated).

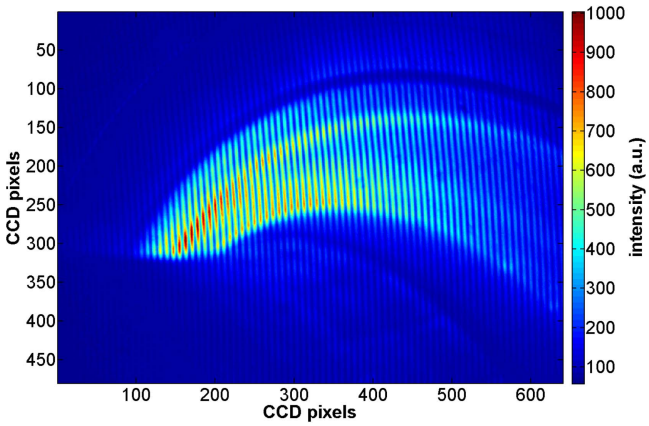

Figure 2. Measured Doppler CIS image of the lower divertor of AUG, modulated with an interference pattern.

emission line. The spatial heterodyne technique has the advantages of a simple, robust optical design and time resolution limited only by the detector framing rate.

The measurement of flows at AUG and W7-X required the development of a stable reliable absolute calibration scheme and associated analysis procedure. A short overview of the CIS principle, set-up and analysis will be presented here; a detailed report on the diagnostic set-up and its analysis is planned in a future publication. Set-ups similar to that used for this work are described in [14, 16–19].

3.1. Coherence imaging principle

The Doppler CIS is a camera-based diagnostic (see schematic in figure 1) measuring a plasma image modulated with an interference fringe pattern, an example of which is shown in figure 2. The recorded fringe phase encodes the centre-of-mass of a narrow-bandpass filtered plasma emission line. It is produced by a birefringent plate in front of the camera, which separates the incident light into an ordinary and extraordinary ray. The phase shift between the two rays is dependent on the orientation of the incident light in relation to the optical axis of the plate as well as the spectral wavelength λ [20]. For the birefringent displacer plate ($\theta = 45°$) used in the set-ups for AUG and W7-X, the phase shift produced can be described as follows (derived from [20], equation (12), assuming small incidence angles and $\theta = 45°$):

$$\Phi = \frac{L}{\lambda}\left[\frac{(n_o^2 - n_e^2)}{(n_o^2 + n_e^2)}\frac{x}{f} + \frac{n_o - n_e}{2}\right] = \frac{L}{\lambda}\left(C \cdot \frac{x}{f} + D\right). \quad (2)$$

Φ is the phase shift between the two separated rays, which is equal to the fringe phase of the modulation pattern. f is the focal length of the objective lens in front of the camera, x is the direction perpendicular to the fringes on the CCD image. n_e and n_o are the extraordinary and ordinary birefringent plate indices. L is the thickness of the plate, λ the centre-of-mass of the observed emission line. By the use of a second polariser and a lens in front of the CCD chip, the rays are reunited and interfere on the CCD chip.

For a single plasma emission or multiplet line to be observed, a narrow ($\approx$2 nm FWHM width) bandpass filter is required to avoid the interference of patterns produced from different emission lines. Two different emission lines cannot be measured at the same time with the same Doppler CIS, unless they are separable from each other in Fourier space (> 100 nm), as was confirmed in a laboratory test with two laser lines. An interesting candidate for such a simultaneous measurement of two emission lines would be e.g. the C II and C III lines at 658 nm and 465 nm, to investigate flow differences of the same species at different ionization stages in the SOL.

The interferometer signal S on the CCD chip is expressed as follows:

$$S = \frac{I_0}{2}(1 + \zeta \cos \Phi). \quad (3)$$

The fringe contrast ζ and phase Φ encode the spectral width and centre-of-mass of the observed emission line, and I_0 is the line intensity. A Fourier transform can be used to mathematically decompose the interferogram S into its three major components, I_0, ζ and Φ, and extract corresponding images of all three quantities separately.

To deduce the particle velocity $v_D = c \cdot \frac{\lambda_0 - \lambda_D}{\lambda_0}$ from a measured, Fourier-analysed phase signal Φ (λ_D) with an unknown wavelength λ_D, the Doppler shift $\Delta\lambda = \lambda_0 - \lambda_D$ is determined by the subtraction of a measured calibration phase image $\Phi(\lambda_0)$ from Φ (λ_D):

$$\Delta\Phi_D = \Phi(\lambda_D) - \Phi(\lambda_0) = \frac{\lambda_0 - \lambda_D}{\lambda_0^2} \cdot L \cdot \left(C \cdot \frac{x}{f} + D\right). \quad (4)$$

Calibration images are made with an integration sphere that is homogeneously illuminated by e.g. a spectral lamp with a known emission line. If $\lambda_{\mathtt{cali}} = \lambda_0$, $\Delta\Phi_D$ is directly linked to the desired Doppler shift $\Delta\lambda_D$. To determine the factor $L \cdot \left(C \cdot \frac{x}{f} + D\right)$ for the $\Delta\Phi \rightarrow \Delta\lambda$-relation, the parameters L, n_o, n_e, x, f need to be known accurately.

If $\lambda_{\mathtt{cali}} \neq \lambda_0$, an additional phase offset $\Phi_V = \Phi(\lambda_0) - \Phi(\lambda_{\mathtt{cali}})$ (cf e.g. [16, 21]) is generated that needs to be considered and subtracted from the measured phase difference $\Delta\Phi_{mc} = \Phi(\lambda_D) - \Phi(\lambda_{\mathtt{cali}})$ to yield the

phase difference of interest, $\Delta\Phi_D$:

$$\Delta\Phi_D = \Delta\Phi_{mc} - \Phi_V \tag{5}$$

In Φ_V, both $\Phi(\lambda_{\text{cali}})$ and $\Phi(\lambda_0)$ are calculated with equation (2), and their difference yields a varying phase value with respect to the pixel position x, depending on the wavelength difference $\lambda_0 - \lambda_{\text{cali}}$. Furthermore, an asymmetric multiplet line structure creates another phase offset Φ_M [14], that can be determined either by summing the line-emissivity-weighted interferograms $S(\lambda_j)$ of each multiplet line j, from which the corresponding phase is determined with a Fourier transform, or according to [21]:

$$\Phi_M = \arg\left(\sum_{j=1}^{n} \mathrm{I}_j \exp\left[2\pi i \frac{\kappa L B}{\lambda_j}\right]\right) - \Phi(\lambda_0), \tag{6}$$

where $B = n_{\text{e}} - n_{\text{o}}$ is the birefringence, I_j the relative emissivity of the multiplet line j, and κ is a factor describing the dependence of B on λ. The spectral centre-of-mass needs to be estimated reliably for each multiplet; otherwise, a phase offset is simulated during the analysis procedure. To determine the spectral centre-of-mass, λ_0, for a multiplet, a statistical distribution among the multiplet energy levels is taken into account to calculate the intensity ratio of each multiplet line (cf [21]). Lines of a multiplet can be measured simultaneously with the Doppler CIS, since all multiplet lines have the same spectral properties (such as Doppler shift of broadening). The intensity ratio was also confirmed with spectral measurements performed by grating spectrometers. Since the observed spectral lines in AUG are multiplets and calibration sources $\lambda_{\texttt{cali}} \neq \lambda_0$ were used, the $\Delta\Phi \rightarrow \Delta\lambda$-relation becomes:

$$\Delta\Phi_D = \Delta\Phi_{mc} + \Phi_M - \Phi_V - \delta\Phi_{\text{e}}. \tag{7}$$

This contains an additional correction term $\delta\Phi_{\text{e}}$, related to uncertainties on the plate parameters: $\Phi_V = \Phi'_V + \delta\Phi_{\text{e}}$ is calculated with an error due to the plate parameters, which can only be determined to a certain accuracy and therefore have uncertainties, which yield $\delta\Phi_{\text{e}}$. For the analysed data from AUG, it was empirically found that $\delta\Phi_{\text{e}} = \Phi_{\texttt{sim}}(\lambda_{\texttt{cali}}) - \Phi_{\texttt{meas}}(\lambda_{\texttt{cali}}) \neq 0$ if the focal length, f, was fitted for the simulations by comparing the simulated and measured calibration phases. A more detailed report of this procedure will be given in a planned future publication.

3.2. Internal Doppler CIS set-up

A top view of the Doppler CIS diagnostic is shown in figure 3. The entire optical set-up was placed in a black box to avoid stray radiation. The birefringent plates and polarizers are mounted onto a fixed rail inside the box. With a motorized flip mirror, the camera view could be changed between the plasma measurement and a calibration sphere. In AUG, a 4.5 m long image fibre bundle had to be used to retrieve light from the torus, the end of which can be seen in the right part of the image in figure 3.

For wavelength calibration, an integrating sphere is used, that is homogeneously illuminated by a spectral lamp. The mirror is flipped into the camera light path for calibration.

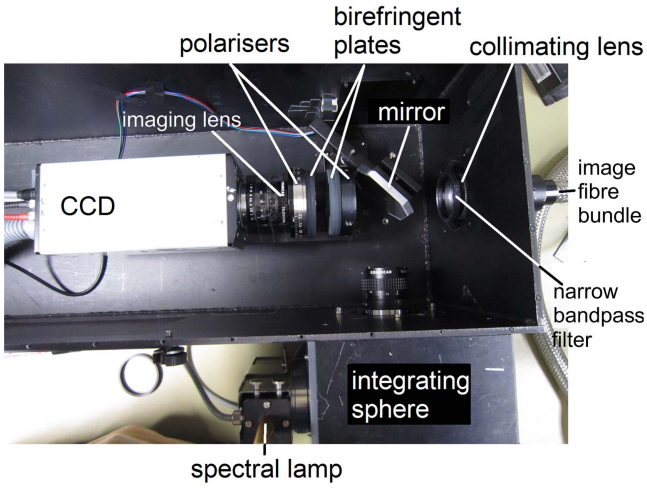

Figure 3. Overview of the Doppler coherence imaging diagnostic for AUG measurements.

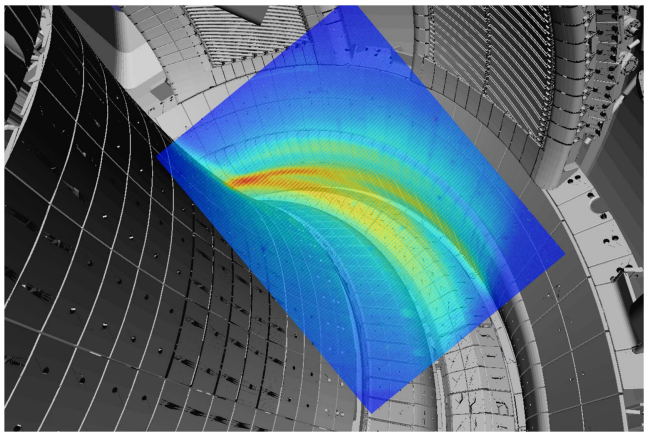

Figure 4. View into the lower AUG divertor with the Doppler CIS camera. A measurement image of the camera is transparently blended into the corresponding CAD image of the AUG wall components.

This enables wavelength calibration directly before and after each measurement, mitigating the effect of environmental changes such as the ambient temperature, which change the refractive indices n_{e} and n_{o}, resulting in phase offsets between calibration and plasma measurement. The assumption of linear temporal changes over the course of a discharge was shown to be sufficient to eliminate all such effects. An example and report on possible phase variations due to ambient plate temperature changes is provided in [1].

3.3. View into AUG

For all measurements presented in this study, the end of the image fibre bundle was located at a vacuum window close to the outboard side of the upper divertor of AUG, viewing obliquely down onto the lower divertor via an $f = 8$ mm objective lens. The view can be seen in figure 4. Using a CAD model of AUG's wall components, a reconstruction of the camera sightlines was made. Selected pixels in the camera images were assigned to x, y, z-values of components

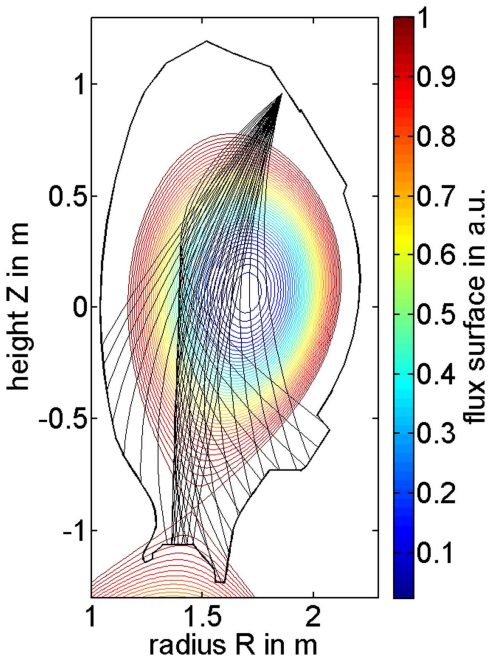

Figure 5. (*R*, *Z*)-projection of a selection of the reconstructed camera sightlines, the first wall of AUG and typical magnetic flux surfaces in the lower divertor configuration.

recognized in the camera image, and a cubic transform was then used to calculate the direction vector of each line-of-sight for each camera pixel. A view of the poloidal (*R*, *Z*)-projection of the sightlines is shown in figure 5.

4. Divertor flows in ASDEX Upgrade

Measurements were carried out for deuterium plasmas mainly in low-recycling divertor regime conditions. To provide insight into ion dynamics, lines of impurity species need to be used, since deuterium does not emit discrete atomic lines when ionized. The choice of lines is limited to intense lines in the divertor SOL, as well as by the availability of calibration lines. For measurements in AUG, the He II line at 468 nm and the C III line at 465 nm were selected, and a Zinc spectral lamp was used for their calibration with a line at 468.014 nm, applied in the analysis equation (7). The uncertainty phase error arising from inaccurate knowledge of plate parameters amounted to an error of $\delta\Phi_e \approx 50°$ for C III or $\delta\Phi_e \approx 30°$ for He II, remaining relatively constant for the analysed discharges. Exposure times of 30−100 ms had to be applied for He II and C III flow measurements; thus, short-time phenomena such as edge localized modes (ELMs) could not be resolved. The measured ion flows and line emission may be strongly influenced by ELMs occurring in the span of a few milliseconds.

The neutral flow of deuterium was also measured to investigate the structure and presence of neutral flows. Ion (or neutral particle) temperature measurements were not performed in AUG with the Doppler CIS. The ion temperature can be determined via the fringe contrast ζ, which is proportional to the spectral width and thus Doppler broadening

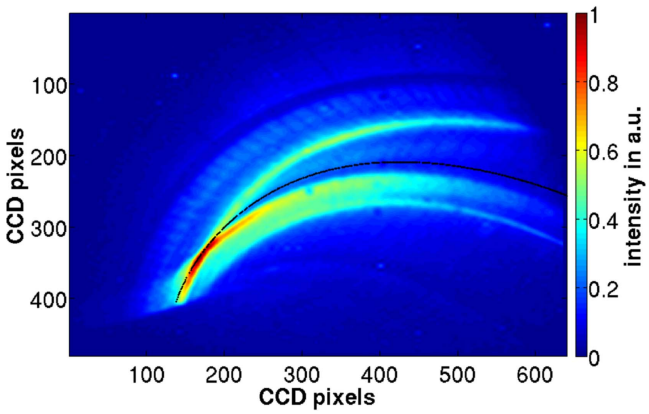

Figure 6. C III emission image measured by the Doppler CIS camera during AUG shot 33666 at $t = 1.78$ s with an exposure time of 30 ms. The black line indicates the position of the X-point.

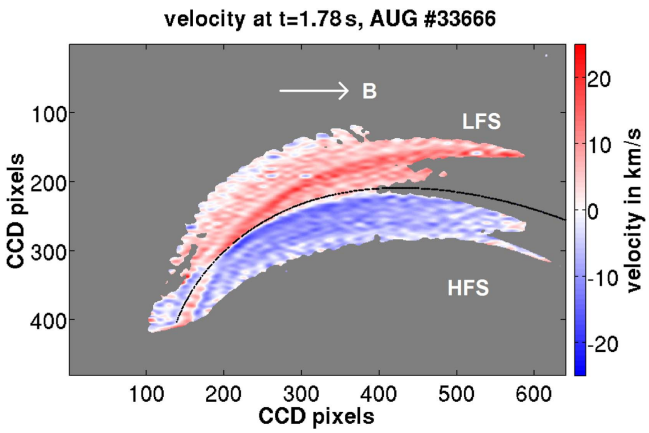

Figure 7. Measured C III flow pattern in the lower divertor of AUG (cf figure 4 for orientation) during an H-mode with applied power of 9 MW in a low-recycling divertor regime. The corresponding emission image is shown in figure 6. All parts of the image where the emission intensity is below 10% of the maximum value are greyed out.

of the observed plasma line. However, the influence of perturbing effects such as Stark, Zeeman broadening or just the background radiation (bremsstrahlung) requires careful analysis and extensive investigation that has not been performed for the AUG measurements.

4.1. Impurity ion flow measurements

Examples of a C III emission and flow measurement are shown in figures 6 and 7. The first image is a Fourier-reconstructed brightness image (low pass filter) of the C III emission. The radiation occurs mainly in the divertor region of AUG, having a distinct radiation pattern dependent on the magnetic flux topology. In this case, there is one strong emission region each on the high-field side (HFS) and low-field side (LFS) close to the divertor plates. The emission pattern is analysed further in section 4.3. Light reflection is clearly visible, revealing the structure of the outer divertor tiles, which consist of tungsten. Reflections could significantly disturb the quantitative analysis of the flows,

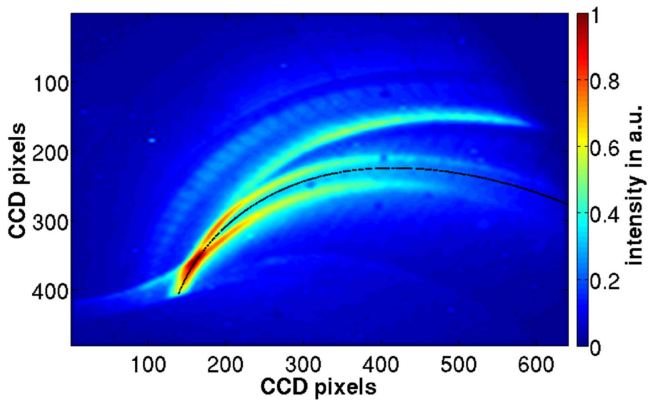

Figure 8. C III emission image measured by the Doppler CIS camera during AUG shot 33678 at $t = 2.33$ s. The black line indicates the position of the X-point. An image exposure time of 30 ms was applied for this measurement.

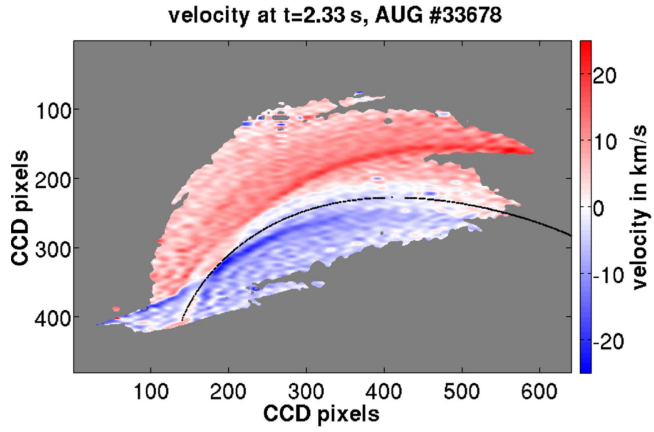

Figure 9. Measured C III flow pattern in the lower divertor of AUG during an H-mode with applied power of 7.5 MW in a high-recycling divertor regime. The corresponding emission image is in figure 8. All parts of the image where the emission intensity is below 10% of the maximum value are greyed out.

especially in regions of weak plasma radiation, but the emission of the plasma can be clearly seen to dominate any reflection in the two main emission stripes that are analysed here. The estimated flow resolution is typically 1–4 km s^{-1}, dependent on the signal-to-noise ratio determined by the fringe contrast and recorded image brightness.

Two major counter-flow areas are observed in figure 7: the carbon ions are moving towards the observer (negative flows/blueshifted) on the HFS and away from the observer in the outer divertor (LFS). At the very left side of the image, the sign of the flow flips above and below the X-Point. In this region, the particle bulk velocity is integrated from both emission areas on the HFS and LFS (cf emission image in figure 6), resulting in a complex mixing of the two. This is an effect of the viewing geometry, since the two emission lines overlay with each other in the diagnostic view. The contour of zero flow observed in the image is located close to the X-point for most of the discharge, indicating that there is no significant systematic error in the absolute calibration. The flow speeds range up to ± 20 km s^{-1} and were relatively stable throughout most of the discharge (the direction of the flows in relation to the magnetic field is analysed in section 4.3).

The poloidal magnetic field B_p points out of the divertor on the HFS and into the target plate on the LFS. At the location of the strike lines, the field lines approach the target at a shallow angle, but from opposite toroidal directions. Thus, the measured flow is directed away from the target plates on both sides, flowing out of the divertor. Forces that usually push impurities away from the plates are the thermal ion and electron temperature gradient forces as well as the impurity pressure gradient force (cf section 2), meaning that one or more of these forces are dominant. The latter one depends strongly on the source of the impurity species. Because the sign is so important to the implications, it was carefully checked in a wavelength scan experiment. Additionally, the approximate Doppler shift of the line can be derived directly from the spatial fringe frequency of the raw image sufficiently accurately to confirm the sign.

Another successfully calibrated C III flow measurement could be performed in a high-recycling regime discharge, and is presented in figure 9. The C III emission pattern (cf figure 8) was slightly different—which is to be expected, since the electron temperature (in the divertor) is decreased in the high-recycling regime. Furthermore, the magnetic field topology was different from the low-recycling case, with a different X-point location. The overall flow pattern and velocities in figure 9 are similar to the low-recycling case, with some local differences. The local flow velocity maximum is higher and the minimum is lower than for the low-recycling case. The position of zero flow is further away from the X-point in the image, due to the different emission pattern during the discharge. The variation of the emission pattern leads to other regions being averaged over. Overall, all the successfully calibrated C III flow measurements (all in the low-recycling regime except the one in figure 9) showed remarkably similar flow speeds, despite varying core plasma parameters ($P_{heat} = 5 - 9$ MW, $n_e = 5 - 8{\cdot}10^{-19}$ m^{-3}). No resonant magnetic perturbations (RMPs) were applied during the C III flow measurements.

A He II flow measurement is presented in figure 10. The measured flows are more noisy than the C III flows due to poor fringe contrast caused by a bad focus of the imaging lens on the CCD. The general flow structure and direction are the same but the flow speeds are only up to ± 15 km s^{-1}, a little less than for C III. While C III is an intrinsic impurity mainly originating from migrated carbon layers on the tungsten divertor tiles, He II is usually most prominent in AUG plasma discharges directly following He glow discharge cleaning. The He II line is also relatively intense when puffed or after boronizations. As for C III in figure 7, the successfully calibrated He II flows were observed in the low-recycling regime.

4.2. Neutral flow measurements

A few Doppler CIS flow measurements were carried out for the D-α line at 656.1 nm, to investigate the existence of a

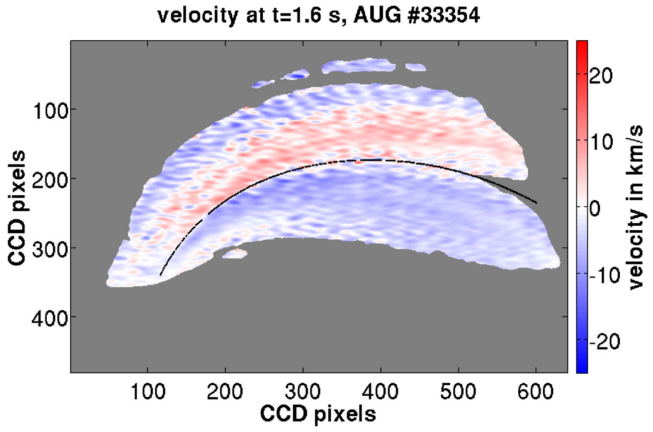

Figure 10. Measured He II flow pattern in the lower divertor of AUG during an H-mode with applied power of 8.5 MW in a low-recycling divertor regime. All parts of the image where the emission intensity is below 10% of the maximum value are greyed out.

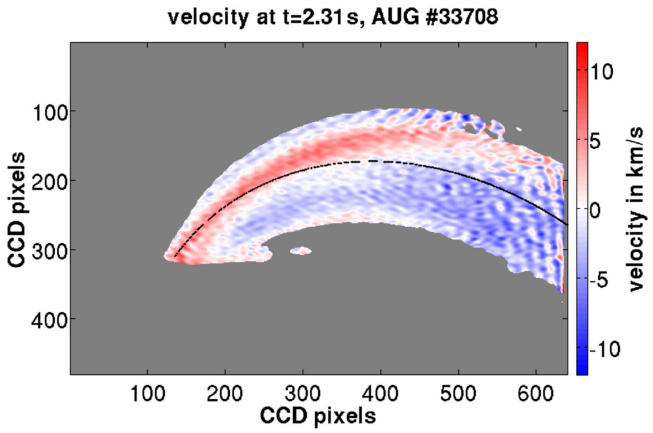

Figure 11. Measured D I flow pattern in the lower divertor of AUG during an L-mode discharge in low-recycling conditions. All parts of the image where the emission intensity is below 10% of the maximum value are greyed out.

directed, neutral bulk flow pattern close to the target plates. For calibration, a diode laser was used, the exact wavelength of which was determined by a spectrometer. D-α is the most intense atomic emission line in the divertor of AUG, and required the shortest possible camera exposure time of 1 ms to avoid saturation. Since D-α has a lower excitation energy than e.g. the ionisation energies of He II or C III and since neutral deuterium is recycled at the wall, it radiates very close to the divertor plates in attached regimes. The D-α radiation pattern was found to be less dependent on the magnetic field topology than for ion species, giving a much broader emission without peaks along the strike lines.

Interestingly, in figure 11, a neutral deuterium flow pattern very similar to the ones observed for He II and C III impurity ions is observed. The neutral deuterium flow speed is significantly less than that of C III and He II and ranges between ± 5 km s^{-1}. The cause of this unexpected neutral flow behaviour is not clear. On the one hand, it is expected that the D-α line emission at the target should primarily originate from recycled neutrals that become excited. However, intuitively, a homogeneous motion of the recycled neutrals away from the plates is expected in high-temperature ($\approx$20 eV) attached conditions rather than the impurity-like pattern observed by the Doppler CIS in figure 11. It could originate from friction of the recycled neutrals with either impurities or plasma background ions; however, these two friction forces are estimated to be weak in attached conditions and counter-directed, since the background plasma ions are expected to flow towards the target plates in an attached regime, whereas both C III and He II were measured to flow away from the plates. Neutrals arising from charge exchange reactions, on the other hand, are expected to contain the momentum they had as ions, explaining the flow pattern, but not the measured flow sign. Plasma ions are generally expected to flow towards the target plates in an attached divertor regime, opposite to the observed impurity and neutral flow, however their flow cannot be directly investigated with the Doppler CIS due to lack of D II atomic emission lines. Charge exchange neutrals should be directed the same way as the background plasma ions.

The measured neutral deuterium flow magnitude and pattern of the Doppler CIS are clear without ambiguity. Studies of the neutral D-α flows in Alcator C-Mod (cf [22], figure 4) also report neutral flows of ± 5 km s^{-1} in the divertor, with the neutral flow directed away from the plates in L-mode conditions, during which the divertor ion temperature is reported to be relatively high ($T_\mathrm{i} \approx 25$ eV).

4.3. Flow component analysis

Since the view of the Doppler CIS camera in AUG was obliquely going down into the lower divertor, the measured flow velocities consist of components both parallel and perpendicular to the magnetic field lines. Parallel as well as perpendicular flow drive mechanisms exist for impurities in the SOL of tokamaks (cf section 2). To deduce the composition for a measured, line-integrated ion flow, a corresponding coordinate system is defined in relation to the magnetic field lines:

- $\vec{\hat{B}}$: **parallel** to the magnetic field lines ($v_\parallel$)
- $\vec{\nabla}\hat{\Psi}_N$ **radial**: perpendicular to the (open) magnetic flux surfaces Ψ (v_r)
- $\vec{\nabla}\hat{\Psi}_N \times \vec{\hat{B}}$ **binormal**: perpendicular to the magnetic field lines, but tangential to the flux surfaces (v_b)

In order to analyse the flow composition, several approximations have to be made:

1. The line-averaged, measured Doppler CIS velocity in a camera pixel, v_m, can be approximated by the line-integrated dot product of the particle velocity $\hat{v}$ and the sightline $\hat{l}$, weighted with the line emission ϵ:

$$\vec{F} = \frac{n_z Z^2}{m_\mathrm{i}^{1/2} T_\mathrm{i}^{3/2}} + \beta_\mathrm{i} \frac{\mathrm{d}(k_\mathrm{B} T_\mathrm{i})}{\mathrm{d}s} + m_z \frac{v_\mathrm{i} - v_z}{\tau_s} + ZeE = 0 \tag{8}$$

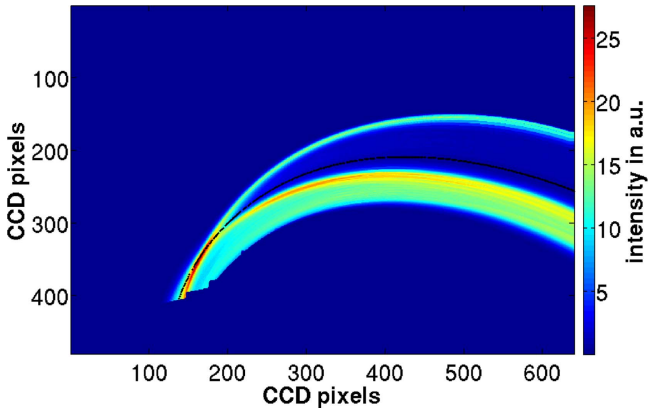

Figure 12. Simulated C III emission image to match the measured image in figure 6.

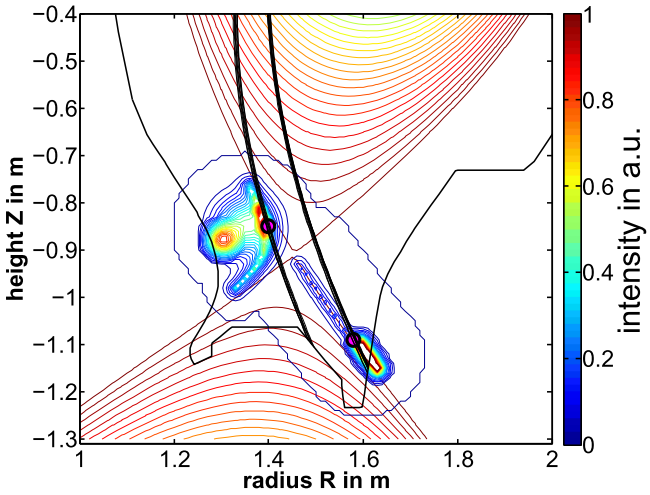

Figure 13. Manually fitted C III emission distribution $\epsilon(R, Z)$ from which the simulated camera image in figure 12 was determined.

2. The line emissivity ϵ needs to be known in (R, Z)-coordinates. This is derived from the emission images of the Doppler CIS.
3. Toroidal axisymmetry is assumed for all edge parameters (such as line emission and particle velocities). This is not true for AUG plasmas with applied RMPs or large error fields.
4. Radial flows v_r are neglected, since the parallel gradients (temperature, pressure) that give rise to radial drifts are relatively small in the low-recycling regime.

With approximations 1 and 4, the measured flow in each camera pixel can be defined as follows in the chosen coordinate system:

$$v_m = \frac{\int \epsilon\,[v_{\|}(\hat{l}\cdot\hat{B}) + v_b(\hat{l}\cdot\{\nabla\hat{\Psi}_N \times \hat{B}\})]\,\mathrm{d}l}{\int \epsilon\,\mathrm{d}l} \tag{9}$$

The flows in the parallel and binormal directions are weighted with the line emission ϵ and the dot product of the sightline with the directional vector in relation to the magnetic field lines. To determine $v_{\|}$ and v_b from the measured flow, the magnetic field topology $(\hat{B}, \nabla\hat{\Psi}_N)$ is determined by the CLISTE code for each discharge and the sightlines $(\hat{l})$ are reconstructed as reported in section 3.3. As an example, the flow components are investigated for the C III flows measured in discharge 33666 (cf figure 7), where no RMPs were applied. The emissivity distribution $\epsilon(R, Z)$ (cf figure 13) is estimated from the measured brightness image in figure 6 and was translated into the camera view in figure 12. The assumed emission distribution $\epsilon(R, Z)$ was manually fitted with five exponentially decreasing, two-dimensional functions so that the simulated emission integral image (figure 12) resembled the measured image (figure 6). Quantitatively, there are deviations of up to 50% between the measured and simulated emission image due to the reflections and vignetting effects, that are not considered in the fitting procedure. These deviations are considered in the error value of the results. For future applications, a fitting algorithm is suggested for inversions of the measured line emissions into the poloidal (R, Z)-plane. The fitted emission pattern in figure 13 corresponds to what is expected for a detached plasma in the inner SOL. The outer divertor is still attached. These differences are observed by bolometers (for the total radiation) [8] (Figure 7), [23] (figure 6, upper image) and are attributed to different densities, the HFS divertor density usually being higher [8].

With the simulated emission $\epsilon(R, Z)$, the line-averaged parallel and perpendicular velocity components $v_{\|}$ and v_b can be determined with one further approximation:

1. For sightlines that integrate over small and single emission areas, the particle velocities are approximately constant: $v_{\|} \approx$ constant and $v_b \approx$ constant.

With the last approximation, equation (9) can be simplified to:

$$v_m = v_{\|}\underbrace{\frac{\int \epsilon(\hat{l}\cdot\hat{B})\,\mathrm{d}l}{\int \epsilon\,\mathrm{d}l}}_{\mathrm{a}} + v_b\underbrace{\frac{\int \epsilon(\hat{l}\cdot\{\hat{B}\times\nabla\hat{\Psi}\})\,\mathrm{d}l}{\int \epsilon\,\mathrm{d}l}}_{\mathrm{b}} \tag{10}$$

Equation (10) has two unknowns, the line-averaged $v_{\|}$ and v_b, for each sightline. The integrals a and b can be calculated for each sightline. Several sightlines that include the same (R, Z)-coordinate were selected and a linear equation system for all these sightlines was set up and solved for $v_{\|}$ and v_b. Furthermore, one has to rely on the toroidal axisymmetry of the tokamak: that at each position of the same R and Z values, the velocity components (and other plasma parameters) stay the same. Equation (10) was solved for the time-averaged value of v_m for each selected sightline during discharge 33666, in which the measured flows remained relatively constant. Two poloidal positions were chosen for the velocity component analysis: one on the HFS at $R = 1.36$ m, $Z = -0.85$ m and one on the LFS at $R = 1.59$ m, $Z = -1.12$ m. These two points are marked in figure 13 and all sightlines which measure these points are shown in the camera image in figure 14.

In figures 15 and 16, the calculated integrals a and b for all selected sightlines, as well as the measured velocity v_m are shown. The two analysed points were selected to satisfy condition 5 (cf figure 13) and condition 3 was checked as

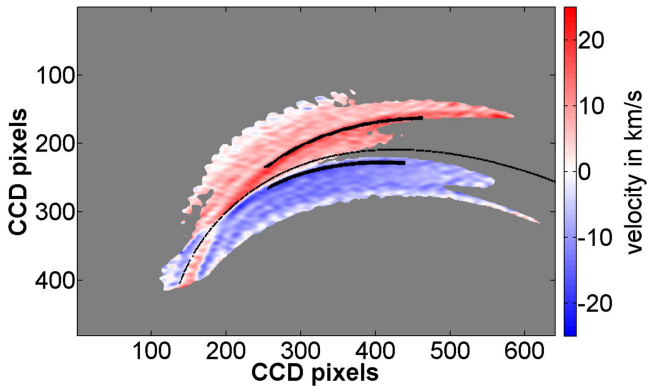

Figure 14. Averaged, line-average C III flow velocity during AUG discharge 33666. The thin black line indicates the position of the X-point; the thick lines mark the sightlines that travel through the selected (R, Z)-coordinates from figure 13. All parts of the image where the emission intensity is below 10% of the maximum value are greyed out.

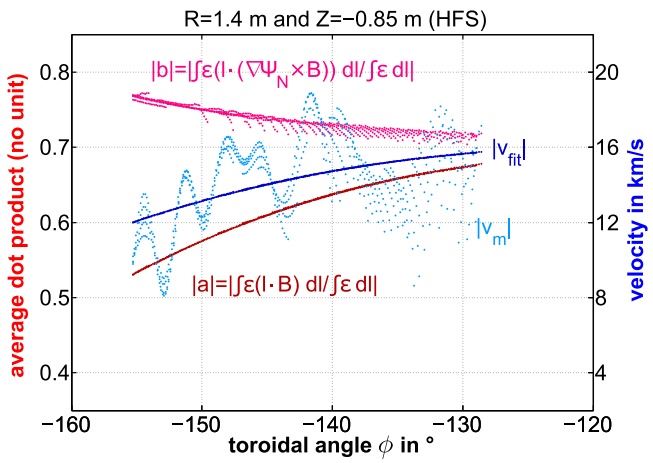

Figure 15. Known parameters of equation (10) for the axisymmetric line on the HFS, as well as the fitted solution for v_m. The left axis shows the scale of the integrals |a| and |b|. The position along the R, Z-line is expressed by the toroidal angle, which increases from right to left in the camera images.

well. By solving the linear equation system for the line-averaged $v_{\|}$ and v_b, the following results were obtained:

- on the HFS-line: $v_{\|} = 25 \pm 4.2$ km s^{-1} and $v_b = -1.6 \pm 3.4$ km s^{-1};
- on the LFS-line: $v_{\|} = -27.5 \pm 1.4$ km s^{-1} and $v_b = 1.5 \pm 1.2$ km s^{-1}.

The signs of $v_{\|}$ and v_b define the flow with respect to the parallel or binormal direction according to equation (10), not to the diagnostic sightlines. The resulting velocity fit from these values is shown in figures 15 and 16. The oscillations of the measured flow data result from the FFT demodulation during the CIS analysis procedure, due to a small size of the inverse Fourier areas because of artifacts. Since the radial direction (defined by $\vec{\nabla}\Psi_N$) points in the same direction as the (positive) radial electric field E_r in the SOL, binormal flows are expected to be positive. However, this is not the case on the HFS. Uncertainties were determined with an error

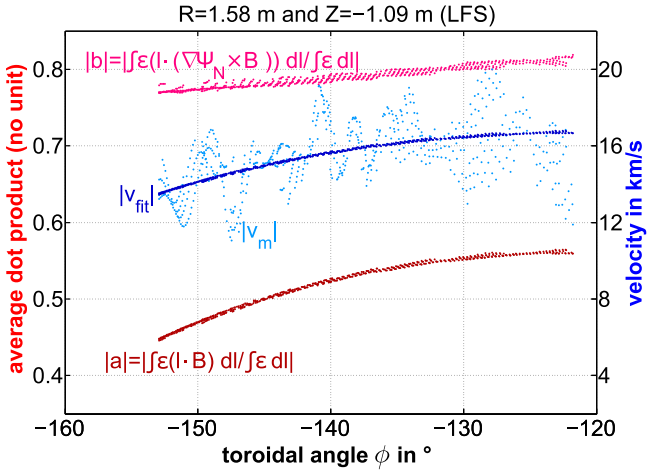

Figure 16. Known parameters of equation (10) for the axisymmetric line on the LFS, as well as the fitted solution for v_m. The left axis shows the scale of the integrals |a| and |b|. The position along the R, Z-line is expressed by the toroidal angle, which increases from right to left in the camera images.

propagation. It included the fitting errors from the linear regression, a deviation $\delta\epsilon$ between the simulated emission pattern and the measured one as well as the systematic error of the velocity signal due to the Doppler CIS analysis procedure, being of the order of ± 500 to 1000 m s^{-1} for the plate configuration in AUG 33666. Since the binormal flow values are nearly the same as the uncertainty of v_m, the sign of the binormal value v_b cannot be trusted. Comparing the parallel and binormal magnitudes, it is implied that the parallel flow was dominant for the measured Doppler CIS C III flow and is in the range of 20−30 km s^{-1}. The perpendicular, binormal flow is at most just a few kilometres per second. Small flows could arise from a combination of radial electric fields in the range of a few kV m^{-1} and diamagnetic drifts due to pressure gradients on the scale of a few millimetres. Between the HFS and LFS, the C III emission (and thus the integration areas) occurs at different distances from the target plates; however, the measured flows were similar.

5. Outlook on Doppler Coherence Imaging in Wendelstein 7-X

In the stellarator W7-X, the island divertor concept [24, 25] is realized and operated for the first time in the operation phase OP1.2a. Two Doppler CIS systems are installed to measure the SOL and divertor flows in W7-X, one looking toroidally and the other poloidally onto the same divertor target. For a detailed report on the Doppler CIS set-ups on W7-X, that profited from the experiences made with the diagnostic in AUG, the reader is referred to [3]. Measurements of these two systems are currently being made, and their results will be published in a future publication.

EMC3-EIRENE simulations were made to estimate the plasma flows in the W7-X island divertor. A versatile synthetic diagnostic module was developed with the code for

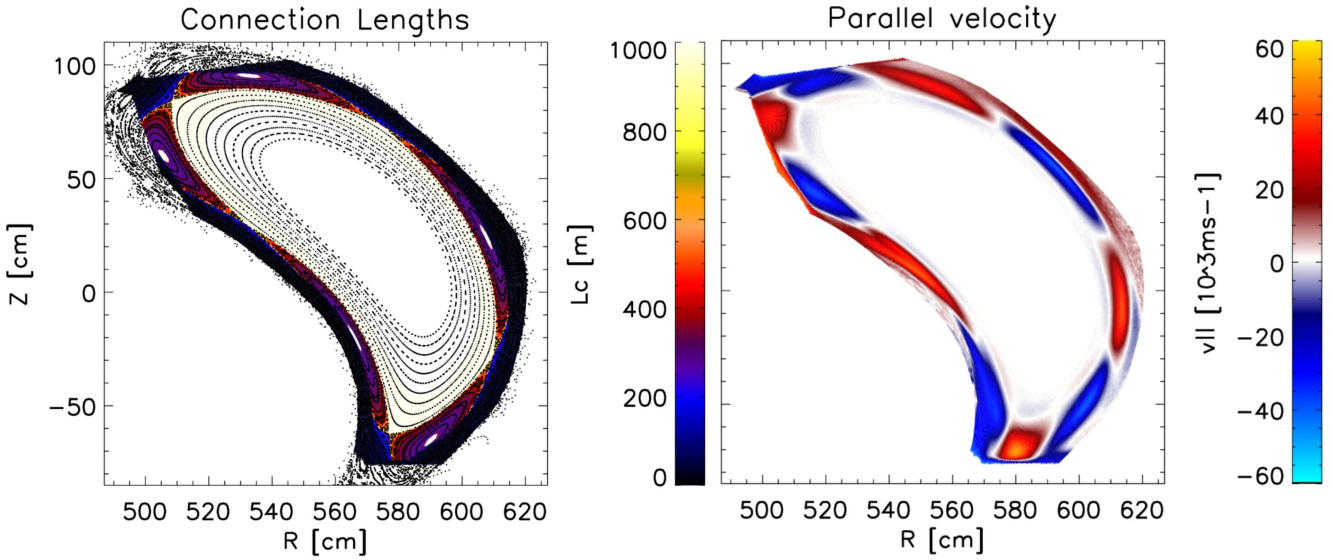

Figure 17. Poloidal cut of the magnetic field connection lengths including a Poincare plot of the five magnetic islands and predicted parallel plasma flow of the EMC3-EIRENE code in W7-X at a toroidal angle of $\phi = 12.3°$. The simulation was made for the standard magnetic field configuration with 2 MW ECRH power, $n_e = 4 \cdot 10^{19}$ m^{-3} SOL density and an anomalous cross-field diffusion $D = 0.5$ m^2 s^{-1}.

W7-X, to simulate and compare with plasma edge diagnostic results such as for the Doppler coherence imaging [11]. Figure 17 shows a poloidal cut of the magnetic connection lengths and EMC3-EIRENE predicted plasma flow velocity distribution in a low-recycling regime. The magnetic $\iota = 1$ standard configuration of W7-X consists of five magnetic independent islands in the SOL. Plasma particles lost from the confined region flow predominantly along the field lines on the surface of the islands in toroidally opposite directions. This causes the particles to stream along the field lines from opposite toroidal directions onto the targets at the position of the strike lines where the targets cut the islands. Similar to LHD [26], it is expected that the islands are filled with particles by perpendicular transport. Due to the radial plasma pressure gradient, parallel flows are driven towards the target plates. This is also the case for other toroidal angles (not shown here). The predicted plasma flows range on the order of several tens of kilometres per second.

Figure 18 shows a simulation of the line-of-sight averaged C III flow distribution from the view of the toroidal Doppler CIS system in the AEQ21 port. A synthetic EMC3-EIRENE module [11] simulated the flow according to:

$$v_m = \int [v_{\|}(\hat{l} \cdot \hat{B})] \mathrm{d}l. \tag{11}$$

This simulation served as a design reference for the CIS systems. In equation (11) and figure 18, the line emission ϵ is not considered yet; it is not what is expected to be measured with the Doppler CIS, which gives a good overview of the flow pattern independent of line emission areas. In case of friction-dominated impurity flows, the impurity flow structure should resemble the plasma flow structure. Despite the complex magnetic field and viewing geometry, a clear plasma counter-flow structure is expected in W7-X due to the island topology. Synthetic EMC3-EIRENE simulation will be used together with the measured flow profiles to gain further

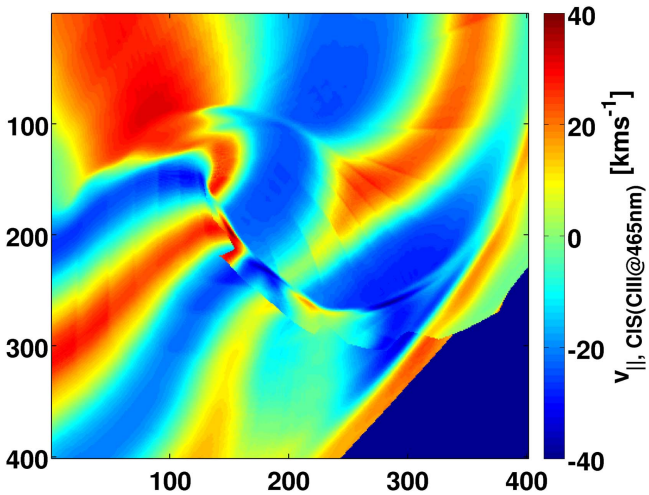

Figure 18. Predicted parallel, line-average C III flow of the EMC3-EIRENE code in W7-X for the Doppler CIS in AEQ21 according to equation (1). The simulation was made for the standard magnetic field configuration with 2 MW ECRH power, $n_e = 4 \cdot 10^{19}$ m^{-3} SOL density and an anomalous cross-field diffusion $D = 0.5$ m^2 s^{-1}.

insight into the physics of the island divertor. Impurity flow structures can differ from the background plasma flow for certain plasma parameters, e.g. if the thermal ion gradient force dominates over the friction force.

Soon to be expected Doppler CIS flow measurements in W7-X will help to verify the EMC3-EIRENE simulations. The general goal of these measurements is to explore the ion velocity flows in the island divertor under diverse conditions, e.g. magnetic field topologies, heating power, detached plasma operation etc. It will be interesting to see whether the impurities are friction-dominated and flow with the plasma towards the targets or not. Another goal is to observe whether for other SOL parameters, impurity flow patterns will significantly change, as e.g. observed in [27]. Since the expected

flows in W7-X are on the same order as in AUG, flow resolution is set to similar values as for the Doppler CIS on AUG ($\Delta\Phi = 10° \rightarrow v_D = 5.6$ km s^{-1}). The spatial resolution of the systems is dependent on the fringe size per camera pixel unit (usually around 4−6 pixels per fringe). The fringe orientation can be varied by rotating the birefringent displacer plates in both systems to vary and adjust the spatial resolution of the diagnostic depending on W7-X plasma parameters.

6. Summary and conclusions

High-quality impurity and neutral flow measurements were carried out with the Doppler CIS for the first time in AUG. The results demonstrate that the diagnostic set-up and analysis works and can be applied for absolutely calibrated flow measurements. The flow measurements were mainly performed in the low-recycling divertor regimes, with flows on the order of 15−20 km s^{-1} for C III, 10−12 km s^{-1}for He II and 5 km s^{-1} for D-α, all pointing away from the divertor target plates. In the case of one C III flow measurement in high-recycling conditions, a local increase in the impurity flow was registered, which is expected due to an increased thermal force resulting from a higher temperature gradient, pushing impurities away from the target plates.

Further Doppler CIS measurements of the impurity flow in the poloidal field divertor of ASDEX Upgrade are planned in different divertor conditions, to investigate whether impurity flow will further vary or even reverse direction under e.g. different divertor regimes. Theory suggests that the impurity flow direction is dependent on e.g. the impurity source or its mass (via the friction force). Therefore, each impurity species can behave individually, which was also confirmed by the diverse flow magnitudes of helium and carbon flows in the AUG divertor. Interestingly, the neutral flow pattern was measured to be very similar to the observed impurity flow patterns. Therefore, more investigations of neutral flows are planned as well, to study what dominates the neutral flow and causes the dependence of the observed pattern on the magnetic topology.

Since the Doppler CIS diagnostic measures along many neighboring lines of sight, the position of which can be easily identified by reference points in the plasma image, it is suitable for tomographic reconstructions in a toroidally symmetric device. A first try of a tomographic reconstruction of the AUG impurity flow measurements has been conducted. It indicates the measured flow amplitude of the system to have been dominated by parallel flows. A stronger physical interpretation of the results would require a dedicated fitting algorithm routine, to reconstruct the measured emission pattern—which, with the trivial reconstruction procedure, is indicated to be of exponentially declining nature, consisting of several emission regions. Furthermore, the line-integration of the physical parameters is simplified, since the linear relation of the (emission-weighted) integral of the local flow is not true for sightlines that average over emission regions with varying flow regions and for flows approaching finite Mach numbers of order of unity. Solving the problem is expected to be challenging, as the line integral becomes non-linear in local flow velocity and requires a knowledge of the temperature distribution as well.

For W7-X, two Doppler CIS systems have been set up for 2D measurements of impurity flows during OP1.2a and later operation phases. SOL and divertor plasma flows simulated by the EMC3-EIRENE code indicate a more complex flow structure than measured in AUG, due to the magnetic island topology.

Acknowledgments

The corresponding author gratefully acknowledges the fruitful correspondences with F Reimold about divertor and SOL flows in tokamaks and T Pütterich, M Cavedon and M Wischmeier for their help in finding an error in the AUG sightline analysis code. Furthermore, the authors would like to thank D Ennis and Auburn University for funding and support for the W7-X Doppler CIS.

This work has been carried out within the framework of the EUROfusion Consortium and has received funding from the Euratom research and training programme 2014-2018 under grant agreement No 633053. The views and opinions expressed herein do not necessarily reflect those of the European Commission.

This work was supported in part by the US Department of Energy (DoE) under grant DE-SC0014210.

ORCID iDs

D Gradic https://orcid.org/0000-0002-6109-9345

References

[1] Lester R *et al* 2016 Coherence imaging for ion temperature and flow measurements in a low-temperature helicon plasma source *Plasma Sources Sci. Technol.* **25** 015025
[2] Feng Y *et al* 2006 Physics of island divertors as highlighted by the example of W7-AS *Nucl. Fusion* **46** 807–19
[3] Perseo V *et al* 2017 Coherence Imaging Spectroscopy systems on Wendelstein 7-X for studies of island divertor plasma behavior *44th EPS Conf. on Plasma Phys.* **41F** 5.103
[4] Grieger G *et al* 1992 Physics optimization of stellarators *Physics Fluids* B **4** 2081
[5] Feng Y *et al* 2011 Comparison between stellarator and tokamak divertor transport *Plasma Phys. Control. Fusion* **53** 024009
[6] Stangeby P C 2000 *The Plasma Boundary of Magnetic Fusion Devices* 1st edn (Bristol: Institute of Physics Publishing)
[7] Jaervinen A E *et al* 2017 Interpretations of the impact of cross-field drifts on divertor flows in DIII-D with UEDGE *Nucl. Mater. Energy* **000** 1–5
[8] Potzel S *et al* 2014 A new experimental classification of divertor detachment in ASDEX Upgrade *Nucl. Fusion* **54** 013001
[9] LaBombard B *et al* 2004 Transport-driven Scrape-Off-Layer flows and the boundary conditions imposed at the magnetic separatrix in a tokamak plasma *Nucl. Fusion* **44** 1047–66

[10] Asakura N 2007 Understanding the SOL flow in L-mode plasma on divertor tokamaks, and its influence on the plasma transport *J. Nucl. Mater.* **363-365** 41–51
[11] Frerichs H *et al* 2016 Synthetic plasma edge diagnostics for EMC3-EIRENE, highlighted for Wendelstein 7-X *Rev. Sci. Instrum.* **87** 11D441
[12] Howard J 1990 Novel scanning interferometer for two-dimensional plasma density measurements *Rev. Sci. Instrum.* **61** 1086
[13] Howard J 2010 Coherence imaging spectro-polarimetry for magnetic fusion diagnostics *J. Phys. B: At. Mol. Opt. Phys.* **43** 144010
[14] Silburn S A *et al* 2014 Coherence imaging of scrape-off-layer and divertor impurity flows in the Mega Amp Spherical Tokamak *Rev. Sci. Instrum.* **85** 11D703
[15] Howard J *et al* 2010 Doppler coherence imaging and tomography of flows in tokamak plasmas *Rev. Sci. Instrum.* **81** 10E528
[16] Samuell C M *et al* 2017 Absolute calibration of Doppler coherence imaging velocity images *J. Instrum.* **12** C08016
[17] Howard J *et al* 2010 Imaging charge exchange recombination spectroscopy on the TEXTOR tokamak *Plasma Phys. Control. Fusion* **52** 125002 10
[18] Howard J *et al* 2011 Coherence imaging of flows in the DIII-D divertor *Contrib. Plasma Phys.* **51** 194–200
[19] Weber T *et al* 2013 Impurity flow measurements at DIII-D using a coherence imaging spectrometer *J. Nucl. Mater.* **438** S1257–60
[20] Veiras F E, Perez L I and Garea M T 2010 Phase shift formulas in uniaxial media: an application to waveplates *Appl. Opt.* **49** 2769–77
[21] Silburn S A 2014 *PhD thesis: A Doppler Coherence Imaging Diagnostic for the Mega-Amp Spherical Tokamak* Durham University
[22] Pitcher C S *et al* 1999 The role of friction in SOL pressure balance in Alcator C-Mod *J. Nucl. Mater.* **266-269** 1009–14
[23] Kallenbach A *et al* 2015 Partial detachment of high power discharges in ASDEX Upgrade *Nucl. Fusion* **55** 053026 (8pp)
[24] Renner H *et al* 2004 Physical aspects and design of the Wendelstein 7-X Divertor *Fusion Sci. Technol.* **46** 318
[25] König R *et al* 2002 The divertor program in stellarators *Plasma Phys. Control. Fusion* **44** 2365–422
[26] Ezumi N *et al* 2009 Experimental observation of plasma flow alternation in the LHD stochastic magnetic boundary *J. Plasma Fusion Res. SERIES* **8** 429–32
[27] Kobayashi M, Morita S and Goto M 2017 2D distribution of hydrogen/impurity radiation and flow formation in stochastic layer during detachment transition in LHD *Nucl. Mater. Energy* **12** 1043–8